Measurement of the Ciliary Beat Frequency through Phase-Contrast Microscopy Image Analysis for the Diagnosis of the Primary Ciliary Dyskinesia: Preliminary Results

E. Parrilla, J.M. Sánchez, M. Armengot, M. Mata, X. Milara, J. Riera and D. Moratal

Abstract—**Primary ciliary dyskinesia (PCD) implies cilia with decreased or total absence of motility, which may result in sinusitis, chronicbronchitis, bronchiectasis and male infertility. A large number of deficiencies detectable on the ultrastructural level give rise to PCD. These infections can be drastically reduced by an precise treatment. An early diagnosis is very important since PCD can cause a permanet lung damage. Diagnosis can be difficult and is based on an abnormal ciliary beat frequency (CBF), accompanied by specific abnormalities of the ciliary axoneme. In this paper, we present a method to determine CBF through the analysis of phase-contrast microscopy imaging acquired using digital high speed video techniques. Beat frequency measurements are made estimating cilia motion by means of an optical flow algorithm. This analysis provides a complete ciliary beat pattern. A previous coregistration process is performed to eliminate cell movements due to cilia motion. The algorithm is tested on several ciliar cell image sequences, concluding that this method is a robust technique to determine CBF.**

Index Terms—**Active contours, Fourier-Mellin transform, optical flow, beat frequency.**

I. INTRODUCTION

PRIMARY ciliary dyskinesia (PCD) is an autosomal recessive inherited disorder affecting approximately 1:10,000 to 1:30,000 individuals [1]-[3]. It causes a defect in the action of the cilia lining the respiratory tract (lower and upper, sinuses, Eustachian tube, middle ear) and fallopian tube. PCD is characterized by the complete absence of mucociliary clearance, leading to respiratory symptoms and signs typically present since birth and predisposing affected individuals to recurrent respiratory infections [4]. Approximately half of sufferers have situs inversus [5]-[7]. Situs inversus combined with chronic sinusitis and bronchiectasis is called Kartageners syndrome.

E. Parrilla and J. Riera are with the Inst. of Multidisciplinary Mathematics, Universidad Politécnica de Valencia, Valencia 46022, Spain (e-mail: edparber@teleco.upv.es).

J.M. Sánchez is with the Electronics Engineering Department, Universitat Politècnica de València, Valencia, Spain

M. Armengot is with the Otorrinolaringology Service of the of the Hospital General Universitario and at the Facultat de Medicina, Universitat de València, Valencia, Spain

M. Mata and X. Milara are with the Fundación para la Investigación of the Hospital General Universitario, Valencia, Spain

D. Moratal is with is with the Center for Biomaterials and Tissue Engineering and with the Electronics Engineering Department, Universitat Politècnica de València, Valencia, Spain

Manuscript received ...; revised ...

Motile cilia play a crucial role in clearing mucus and debris from the airways under normal conditions, as can be seen in patients with abnormal airway ciliary beating caused by primary ciliary dyskinesia [8], [9]. Motile cilia also play a role in circulating spinal fluid in the ventricles of the brain, where abnormal ciliary beating has recently been linked to hydrocephalus and other developmental cerebral abnormalities [10], [11].

Despite persistent symptoms, and often attendance at ear, nose, and throat and respiratory clinics, many patients with PCD are not diagnosed until later in life [12], by which time permanent lung damage has occurred [13]. Early and accurate diagnosis is important, because once made, lung function can be maintained with specialist respiratory care [14]-[16]. The diagnosis of PCD is traditionally made on the basis of a supportive clinical history and an abnormal ciliary beat frequency (CBF). The most commonly used techniques (the modified photodiode [17] or photomultiplier method [18]) to measure CBF use an indirect method and do not provide information on ciliary beat pattern. New high-resolution digital high speed video (DHSV) imaging has allowed the precise beat pattern of cilia [19].

A commonly used method to estimate CBF using a DHSV has been explained in [20], [21]. This method computes the Fast Fourier Transform (FFT) of the intensity signals in a window of 3x3 pixels centred on a selected pixel above the cilium. This technique does not consider the global movement of all cilia and local illumination changes can affect the results. On the other hand, this method is not valid when the cell is moving due to its own ciliar beat.

In this paper, we present a method to measure CBF based on the analysis of the cilia global movement by means of optical flow algorithms. A coregistration process is also implemented to eliminate the cell movement. The main modules in the system are summarized in Fig.1. In next section, functionality of each block is described.

II. METHOD

A. Image Acquisition

Ciliar cells were mounted onto the stage of a Nikon Eclipse TE100 microscope, by using a 40x Nikon lens with a final optical gain of 400x. The microscope was connected to a CCD camera (Digital Quad High Speed Progressive Scan Camera,
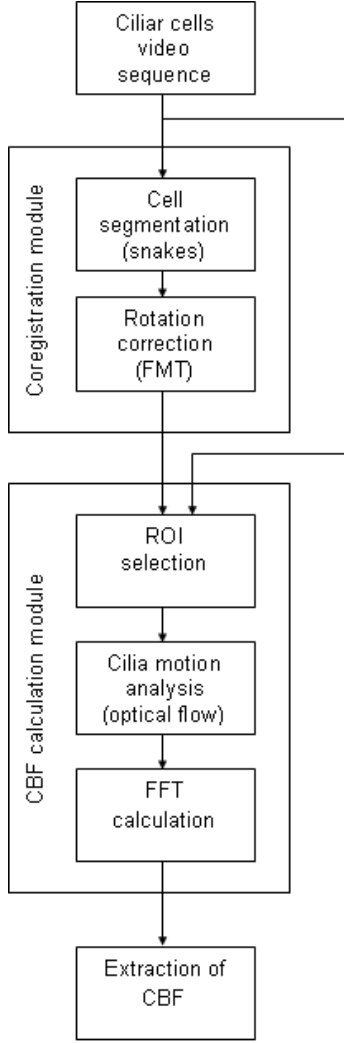
Fig. 1.   System flow diagram

JAI CV-A33 CL) that records the images with a matrix size of 649x494 pixels, and a rate of 120 frames per second.

Images were acquired into a HP Workstation xw6200 Xeon 3.4 GHz with 2Gb of RAM system by means of an image acquisition board (NI PCIe-1429, Full Configuration Camera Link Image Acquisition).

B. Coregistration

Ciliated samples are placed in a liquid solution. Therefore, ciliar beat can cause a movement of the cells to analyze. In general, there are two groups: isolated cells that have a rotation movement, and cells that are sticked on other components of the solution and keep still. In the first case, it is necessary to eliminate this rotation movement to estimate CBF.

1) Cell segmentation: For initiating the coregistration process, it is necessary to localize the cell to analize. We propose an automatic segmentation method based on gradient vector flow snakes to perform this task. A snake is an energy-minimizing spline guided by external constraint forces and influenced by image forces that pull it toward features such as lines and edges [22]. Instead of exploiting only image

information as low-level edge-detection techniques do, snakes also use information about the boundaries as part of an optimisation procedure. Snakes are active contour models: they lock onto nearby edges, localizing them accurately.

The active-contour model involves vertices connected by edge segments with, in general, two associated force terms. The internal force is computed based on the local shape of the contour. The external force (or image force) that drives the active contour to the boundary can be based on any conventional edge-detection technique. The internal and external forces may be weighted differently.

Mathematically, a snake can be defined in discrete form as a curve $\mathbf{x}(s) = [x(s), y(s)]$, $s \in [0, 1]$ that moves through the spatial domain of an image to minimize the energy functional

$$E = \int_0^1 \frac{1}{2}(\alpha \left| \mathbf{x}'(s) \right|^2 + \beta \left| \mathbf{x}''(s) \right|^2) + E_{ext}(\mathbf{x}(s))ds \quad (1)$$

where α and β are weighting parameters that control the active contour's tension and rigidity respectively, and govern the effect of the derivatives of $\mathbf{x}(s)$. The external energy function E_{ext} is derived from the image so that it takes on its smaller values at the features of interest such as boundaries.

A snake that minimizes (1) must satisfy the Euler equation

$$\alpha \mathbf{x}''(s) - \beta \mathbf{x}''''(s) - \nabla E_{ext} = 0 \quad (2)$$

where $F_{int} = \alpha \mathbf{x}''(s) - \beta \mathbf{x}''''(s)$ and $F_{ext} = -\nabla E_{ext}$ comprise the components of a force balance equation such that $F_{int} + F_{ext} = 0$.

Xu and Prince [23] proposed Gradient Vector Flow (GVF) to improve the capture range of the image force. GVF involves a vector field derived by solving a vector diffusion equation which diffuses the gradient vectors of a grey-level image. The solution for the GVF vector field involves a combination of Laplacian and gradient terms, and a blending factor is used for governing the trade-off between them. GVF snakes replace the potential force $-\nabla E_{ext}$ by the gradient vector flow field. The GVF field can be defined as the vector field $\mathbf{v}(x, y) = (u(x, y), v(x, y))$ that minimizes the energy functional

$$\epsilon = \int \int \mu(u_x^2 + u_y^2 + v_x^2 + v_y^2) + \left| \nabla f \right|^2 \left| \mathbf{v} - \nabla f \right|^2 dxdy \quad (3)$$

where the parameter μ is a regularization parameter governing the tradeoff between the first and the second term. This parameter should be set according to the amount of noise present in the image (more noise, increase μ).

Using the calculus of variations [24], the GVF can be calculated by solving the next Euler equations

$$\mu \nabla^2 u - (u - f_x)(f_x^2 + f_y^2) = 0$$
$$\mu \nabla^2 v - (v - f_y)(f_x^2 + f_y^2) = 0 \quad (4)$$

The set of equations (4) can be solved by considering u and v as functions of time and computing

$$u_t(x,y,t) = \mu \nabla^2 u(x,y,t) - (u(x,y,t) - f_x(x,y))$$
$$\cdot (f_x(x,y)^2 + f_y(x,y)^2)$$
$$v_t(x,y,t) = \mu \nabla^2 v(x,y,t) - (v(x,y,t) - f_y(x,y))$$
$$\cdot (f_x(x,y)^2 + f_y(x,y)^2) \quad (5)$$

The steady-state solution (as $t \to \infty$) of these linear parabolic equations is the desired solution of the Euler equations (4). The equations in (5) are known as generalized diffusion equations. A stable explicit finite difference implementation for solving the steady-state solution of (5) was given in [25].

An example of GVF snake segmentation is given in Fig.2. Control points used in the first frame of the sequence to initialize the algorithm are shown in Fig.2(a). These points are selected as a first contour estimation. Subsequently, an iterative process is performed to adapt the snake to the cell contour; see Fig.2(b). In Fig.2(c), we can observe the final cell segmentation after 50 iterations.
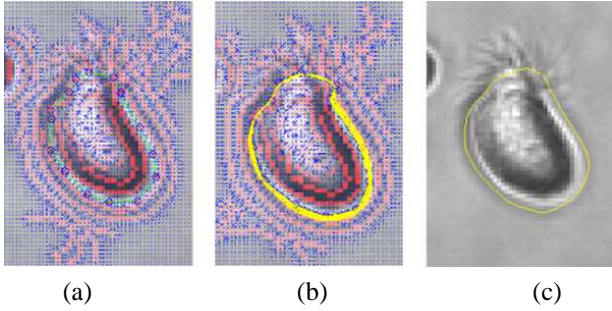

Fig. 2. Cell segmentation process. (a) Selected control points. (b) Snake adapting to the contour cell. (c) Cell segmentation (after 50 iterations).

In our method, the segmentation of the first frame is used as a first contour estimation of the other sequence frames. Using this initial estimation, the algorithm computes an iterative process to perform the cell segmentation in each frame. In Fig.3, we can observe the cell segmentation in different frames of a video sequence.
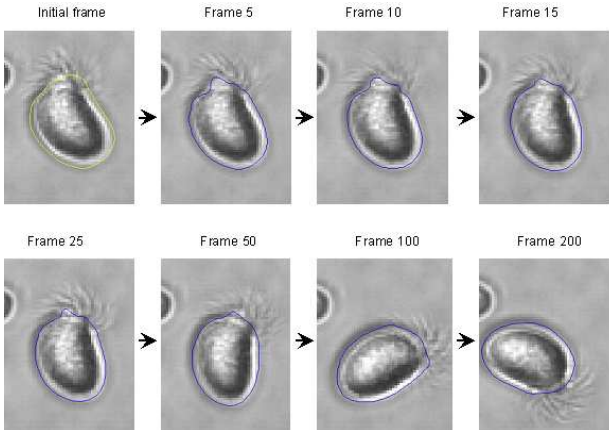

Fig. 3. Cell segmentation in different frames of the video sequence.

2) Rotation Correction: Segmented images are used to center the cell in the middle of the images. Once the cell is centered, for each frame, the rotation is corrected by using a method based on Fourier-Mellin transforms [26]. The solution of this problem consists in finding the angle that each frame forms with the first frame of the sequence.

We consider a function of two variables in polar coordinates $f(r,\theta)$, $\forall (r,\theta) \in R_+^* \cdot S^1$ where r is the radial variable and θ is the angular variable.

For this function, the Analytic Fourier-Mellin Transform (AFMT) is defined as [27]

$$M_{f_\sigma}(k,v) = \frac{1}{2\pi} \int_0^\infty \int_0^{2\pi} f(r,\theta) r^{\sigma-iv} e^{-ik\theta} d\theta \frac{dr}{r} \quad (6)$$

where σ is a positive constant that prevents the divergence when $r \to 0$.

An interesting property of the AFMT is the translation theorem in log-polar coordinates. For two functions with $g(r,\theta) = f(\alpha r, \theta + \beta)$, this theorem is

$$M_{g_\sigma}(k,v) = \alpha^{-\sigma+iv} e^{ik\beta} M_{f_\sigma}(k,v) \quad (7)$$

where α and β are constants that represent scale and rotation changes, respectively.

On the other hand, we can define the following function

$$E_{f,g}(\rho,\varphi) = \left(\int_0^\infty \int_0^{2\pi} r^{2\sigma} |f(r,\theta) - g(\rho r, \theta + \varphi)|^2 d\theta \frac{dr}{r} \right)^{\frac{1}{2}} \quad (8)$$

This function measures, in all points of parameter space (ρ,φ), the similarity between both functions.

Applying Parseval's equality [28] on equation 8, we obtain

$$E_{f,g}(\rho,\varphi) = \left(\int_{-\infty}^{+\infty} \sum_{k \in Z} \left| M_{f_\sigma(r,\theta)}(k,v) - M_{g_\sigma(\rho r,\theta+\varphi)}(k,v) \right|^2 dv \right)^{\frac{1}{2}} \quad (9)$$

Finally, applying the translation theorem (equation (7)), we have

$$E_{f,g}(\rho,\varphi) = \left(\int_{-\infty}^{+\infty} \sum_{k \in Z} \left| M_{f_\sigma}(k,v) - \rho^{-\sigma+iv} e^{ik\varphi} M_{g_\sigma}(k,v) \right|^2 dv \right)^{\frac{1}{2}} \quad (10)$$

We now assume that there is not variation in scale ($\rho = 1$). In this case, equation (10) yields

$$E_{f,g}(\varphi) = \left(\int_{-\infty}^{+\infty} \sum_{k \in Z} \left| M_{f_\sigma}(k,v) - e^{ik\varphi} M_{g_\sigma}(k,v) \right|^2 dv \right)^{\frac{1}{2}} \quad (11)$$

If $f(r,\theta)$ denotes the intensity function of an image and $g(r,\theta)$ is the intensity function of the same image but rotated,

the angle φ_m that minimizes equation 11 is the angle that both images form. In Fig.4, we can observe different frames of a moving cell video sequence with rotation correction.

An advantage of this method is that the calculation of the AFMT is very fast because, with a change of variables, it can be converted in a FFT.
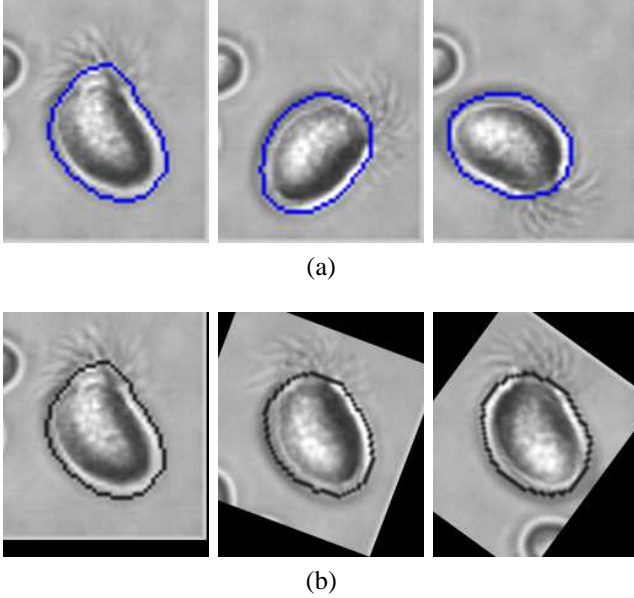

(a)

(b)

Fig. 4. Rotation correction. (a) Different frames of a video sequence with a rotating cell. (b) Frames after eliminating the rotation movement.

C. Measurement of CBF

Once the movement of the cell has been eliminated, a region of interest (ROI) is selected. This ROI includes all cilia and their movement along all the sequence. For the CBF analysis, a motion estimation technique based on optical flow has been implemented.

For computing the optical flow of a frame of a video sequence, it is necessary to assume that intensity variations of the image are only caused by displacements of the objects, without considering other causes such as changes of illumination. This hypothesis, proposed initially by Horn and Schunck [29], supposes that present intensity structures in the image, at local level, stay constant throughout the time, at least during small temporal intervals. Formally, if $I(\bar{x}, t) = I(x(t), y(t), t)$ denotes the continuous space-time intensity function of an image, it has to be fulfilled that

$$I(x(t), y(t), t) \approx I(x(t + \Delta t), y(t + \Delta t), t + \Delta t) \quad (12)$$

By expanding the right-hand side of equation (12) using the Taylor series yields

$$I(t) \approx I(t) + \frac{dI(t)}{dt}\Delta t + O^2(\Delta t) \quad (13)$$

that is,

$$\frac{dI}{dt} = 0 \quad (14)$$

where $O^2(\Delta t)$ are the 2nd and higher order terms, which are assumed to be negligible. Finally, applying the Chain rule, we obtain the optical flow equation

$$\frac{\partial I}{\partial x}\frac{dx}{dt} + \frac{\partial I}{\partial y}\frac{dy}{dt} + \frac{\partial I}{\partial t} = 0 \quad (15)$$

or, in another way

$$I_x u + I_y v + I_t = 0 \quad (16)$$

where I_x, I_y are the components of the spatial gradient ∇I, I_t denotes partial differentiation with respect to time and $\mathbf{v} = (u, v)$ denotes the components of the image velocity field. The distribution of the velocity in each point of the image is known as the optical flow.

Constraint (16) is not sufficient to solve the optical flow equation for a given frame. The problem is ill-posed because we have to compute two components, u and v, and we only have one equation. This phenomenon is known as the aperture problem. It is necessary to consider additional restrictions to the problem to estimate the motion at every image location.

There are many techniques for computing the optical flow, which differ one from each other in the different assumptions that are taken into account to determine the solution. In this work, we have used the Proesmans algorithm [30].

Proesmans et al. present a method similar to that of Horn and Schunck. The main differences are that a matching process is incorporated into the constraint equation and a method for dealing with discontinuous flows is introduced. In order to evaluate the current flow estimate, Proesmans et al. look at the correspondences suggested by the current flow estimate. For each point, (x, y), in the first image the estimated optical flow, (u, v), can be used to find a corresponding point, $(x + u, y + v)$, in the second image. If the flow estimate is good then the brightness at these two points should be similar. If the brightnesses are not the same then the flow estimate is moved along the image gradients in order to correct for the difference. Proesmans et al. use a process known as anisotropic diffusion to smooth the flows. The application of anisotropic diffusion means that the local averages of the flow components are not simple averages but are weighted by a consistency map. Unlike the normal smoothing process, this can maintain discontinuities in the flow but still retains a high level of continuity in local regions.

This approach is basically a merger of correlation and differential techniques. The proposed algorithm computes optical flow using a coupled set of non linear equations

$$\frac{\partial u}{\partial t} = \nabla^2 u - \lambda I_x (I_x u + I_y v + I_t(\tilde{u}, \tilde{v}))$$
$$\frac{\partial v}{\partial t} = \nabla^2 v - \lambda I_y (I_x u + I_y v + I_t(\tilde{u}, \tilde{v})) \quad (17)$$

where $(\tilde{u}, \tilde{v})$ can be any estimate of the velocity components.

In Fig.5, a ROI selection and an example of frame-by-frame optical flow calculation are given. Optical flow computation produces an individual displacement signal $d_i(t)$ for each pixel i along time. The approach used to estimate CBF computes the sum of the FFT of these signals
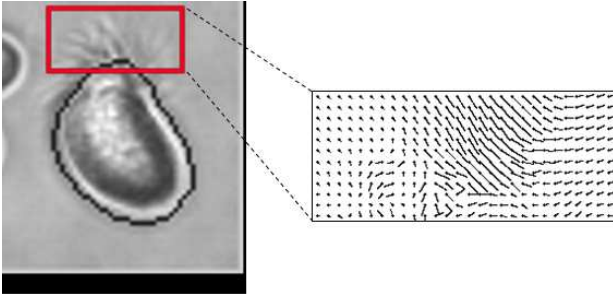
Fig. 5. ROI selection and optical flow calculation for two frames of the video sequence.

$$Y(f) = \frac{1}{NL} \sum_{i=1}^{N} |FFT(d_i(t))| \qquad (18)$$

where N is the number of signals or number of pixels in the ROI and L is the length of the signals or number of analyzed frames.

III. RESULTS

In this section, we present experiments that apply the exposed technique to images from real ciliar cells. Our method has been tested on three phase-contrast microscopy image sequences. Analyzed cells can be observed in Fig.6.
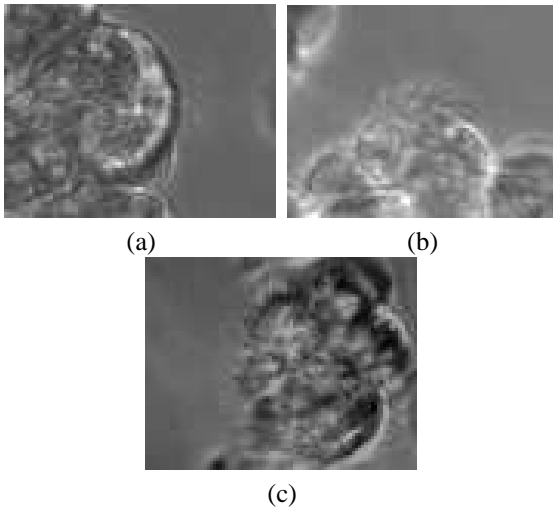

(a)   (b)

(c)

Fig. 6. Analyzed cell video sequences.

In Fig.7, we can observe the CBF calculation for cell in Fig.6(a). In this case, the CBF value is 6.02Hz. We can see others frequency components that correspond to harmonics of the fundamental frequency.

In the case of cell in Fig.6(b), analysing the sum of the FFTs, we obtain a CBF value of 3.4Hz; see Fig.8.

The CBF calculation for cell in Fig.6(c) is given in Fig.9. The computed CBF value is 7.96Hz.

All examples have been analyzed using the method described in [20], [21], obtaining similar results (6Hz, 3.45Hz and 7.9Hz respectively for cells in Fig.6).
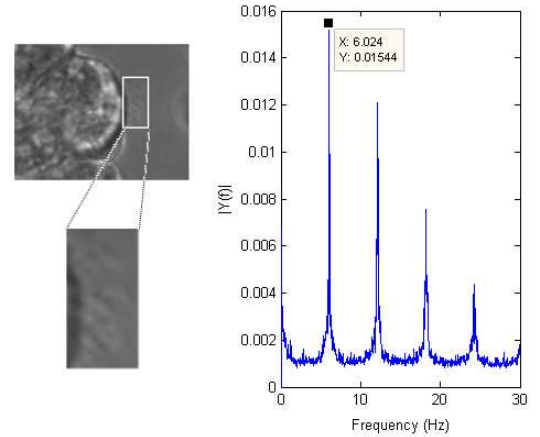

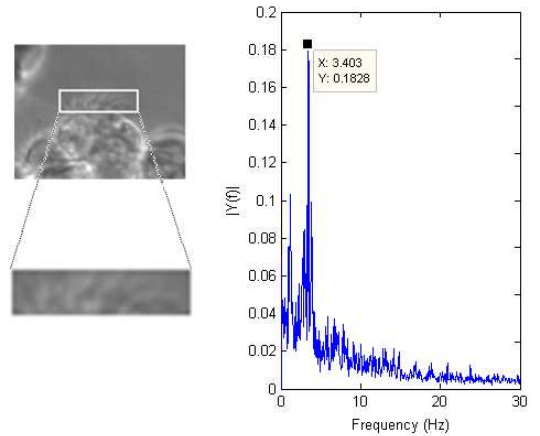Fig. 7. Frequency analysis result for Fig.6(a) cell image using a 15x33 pixel ROI.

Fig. 8. Frequency analysis result for Fig.6(b) cell image using a 47x12 pixel ROI.

IV. CONCLUSION AND FUTURE WORK

In this paper, we present a system for analysis of motion in ciliar cells in order to estimate CBF. Studying cilia movement is a very challenging task because it is necessary to previously eliminate undesirable movements of the own cell. For this reason, we have implemented a coregistration process based on cell segmentation and Fourier-Mellin transforms. This technique provides a fast and robust method for eliminating rotations.

For analysis of cilia motion, an optical flow algorithm has been used. Compared to existing approaches in this field, our approach is a substantial improvement for studying the cilia movement. Conventional methods, which analyze the intensity variations of an isolated pixel, are not robust to noise and illumination changes due to the own cilia movement. These methods estimate CBF using local information. On the other hand, our method estimate CBF extracting the movement of all pixels that belong to cilia. This global information can also be used to obtain a complete pattern of movement and detect other possible anomalies in the movement and characteristics
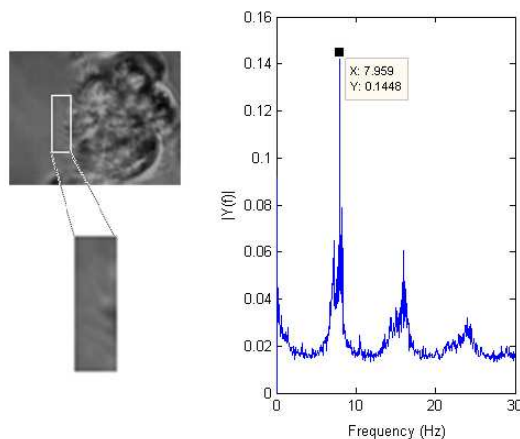
Fig. 9. Frequency analysis result for Fig.6(c) cell image using a 10x28 pixel ROI.

of cilia.

REFERENCES

[1] B. A. Afzelius, "A human syndrome caused by immotile cilia," *Science*, vol. 193, no. 4250, pp. 317-319, 1976.
[2] B. A. Afzelius, "The immotile-cilia syndrome and other ciliary diseases," *Int Rev Exp Pathol*, vol. 19, pp. 1-43, 1979.
[3] B. A. Afzelius, "Immotile cilia syndrome: past, present, and prospects for the future," *Thorax*, vol. 53, pp. 894-897, 1998.
[4] M. Armengot et al., "Discinesia ciliar primaria. Ciliopatías," *Acta Otorrinolaringol Esp.*, doi:10.1016/j.otorri.2009.01.013, 2009.
[5] A. Bush, P. J. Cole, M. Hariri, I. Mackay, G. Phillips, C. OCallaghan et al., "Primary ciliary dyskinesia: diagnosis and standards of care," *Eur Respir J*, vol. 12, pp. 982-988, 1998.
[6] D. V. Schidlow, "Primary ciliary dyskinesia (the immotile cilia syndrome)," *Ann Allergy*, vol. 73, pp. 457-468, 1994.
[7] M. Meeks, A. Bush, "Primary ciliary dyskinesia," *Pediatr Pulmonol*, vol. 29, pp. 307-316, 2000.
[8] H. Mitchison, M. Salathe, M. Leigh, J. Carson, "Primary ciliary dyskinesia," in *Encyclopedia of Respiratory Medicine*, ed. G. Laurent and S. Shapiro, New York, Elsevier, pp. 485-489, 2006.
[9] W. Moller, K. Haussinger, L. Ziegler-Heitbrock, J. Heyder, "Mucociliary and long-term particle clearance in airways of patients with immotile cilia," *Respir. Res.*, vol. 7, pp. 10, 2006.
[10] B. Banizs, M. M. Pike, C. L. Millican, W. B. Ferguson, P. Komlosi et al, "Dysfunctional cilia lead to altered ependyma and choroid plexus function, and result in the formation of hydrocephalus," *Development*, vol. 132, pp. 5329-5339, 2005.
[11] K. Sawamoto, H. Wichterle, O. Gonzalez-Perez, J. A. Cholfin, M. Yamada et al, "New neurons follow the flow of cerebrospinal fluid in the adult brain," *Science*, vol. 311, pp. 629-632, 2006.
[12] J. A. Turner, C. W. Corkey, J. Y. Lee, H. Levison, J. Surgess, "Clinical expression of immotile cilia syndrome," *Pediatrics*, vol.67, pp. 805-810, 1981.
[13] A. Ellerman, H. Bisgaard, "Longitudinal study of lung function in a cohort of primary ciliary dyskinesia," *Eur Resp J*, vol. 10, pp. 2376-2379, 1997.
[14] C. W. Corkey, H. Levison, J. A. P. Turner, "The immotile cilia syndrome. A longitudinal survey," *Am Rev Respir Dis*, vol. 124, pp. 544-589, 1981.
[15] M. A. Greenstone, P. Stanley, P. Cole, I. Mackay, "Upper airway manifestations of primary ciliary dyskinesia," *J Laryngol Otol* vol. 99, pp. 985-991, 1985.
[16] P. J. Hadfield, J. M. Rowes-Jones, A. Bush, I. Mackay, "Treatment of otitis media with effusion in children with primary ciliary dyskinesia," *Clin Otolaryngol*, vol. 22, pp. 302-306, 1997.
[17] H. Teichtahl, P. L. Wright, R. L. Kirsner, "Measurement of in vitro ciliary beat frequency: a television-video modification of the transmitted light technique," *Med Biol Eng Comp*, vol. 24, pp. 193-196, 1986.
[18] T. Dalhamn, R. Rylander, "Frequency of ciliary beat measured with a photosensitive cell," *Nature*, vol. 196, pp. 592-593, 1962.
[19] M. Chilvers, C. O'Callaghan, "Analysis of ciliary beat pattern and beat frequency using digital high-speed imaging: comparison with the photomultiplier and photodiode methods," *Thorax*, vol. 55, pp. 314-317, 2000.
[20] M. Salathe, R. J. Bookman, "Mode of Ca2+ action on ciliary beat frequency in single ovine airway epithelial cells," *J Physiol*, vol. 520, no. 3, pp. 851-865, 1999.
[21] Z. Sutto, G. E. Conner, M. Salathe, "Regulation of human airway ciliary beat frequency by intracellular pH," *J Physiol*, vol. 560, no. 2, pp. 519-532, 2004.
[22] M. Kass, A. Witkin, D.Terzopoulos, "Snakes: Active contour models," *Int. J. Computer Vision*, vol. 1, no. 4, pp. 321-331, 1987.
[23] C. Xu, J. L. Prince, "Gradient vector flow: a new external force for snakes," *IEEE Conference Proceedings on Computer Vision and Pattern Recognition*, pp. 66-71, 1997.
[24] R. Courant, D. Hilbert, "Methods of Mathematical Physics," *Interscience*, NewYork, vol. 1, 1953.
[25] C. Xu, J. L. Prince, "Snakes, shapes, and gradient vector flow," Technical Report JHU-ECETR96-15, The Johns Hopkins University, 1996.
[26] D. Casasent, D. Psaltis, "Scale invariant optical transform," *Optical Engineering*, vol. 15, no. 3, pp. 258-261, 1976.
[27] S. Derrode "Représentation de formes planes à niveaux de gris par différentes approximations de Fourier-Mellin analytique en vue d'indexation de bases d'images," Ph. D. dissertation, ENST-Bretagne, 1999.
[28] L. W. Johnson, R. D. Riess, "Numerical Analysis," Addison-Wesley, 1982.
[29] B. K. P. Horn, B. G. Schunck, "Determining optical flow," *Artificial Intelligence*, vol. 17, no. 1-3, pp. 185-203, 1981.
[30] M. Proesmans, L. Van Gool, E. Pauwels, A. Oosterlinck, "Determination of optical flow and its discontinuities using non-linear diffusion," in *3rd Eurpoean Conference on Computer Vision, ECCV'94*, vol. 2, pp. 295-304, 1994.